Insights into pāhoehoe lava emplacement using visible and thermal structure-from-motion photogrammetry

Sébastien Biass[1,2], Tim R. Orr[3,4], Bruce F. Houghton[1], Mathew R. Patrick[3], Mike R. James[5], Nicolas Turner[1],

[1] *Geology and Geophysics, University of Hawai'i at Mānoa, Honolulu, Hawaii, USA*

[2] *Earth Observatory of Singapore, Nanyang Technological University, Singapore*

[3] *U.S. Geological Survey, Hawaiian Volcano Observatory, Hawaii National Park, Hawaii, USA*

[4] *U.S. Geological Survey, Alaska Volcano Observatory, Anchorage, Alaska, USA*

[5] *Lancaster Environment Centre, Lancaster University, Lancaster, UK*

Corresponding author: Sébastien Biass (sbiasse@ntu.edu.sg)

Key points

- We document the first 3 months of a pāhoehoe flow, from its initial crust-free channel into a compound field fed by a tube system;
- Visible and thermal aerial images describe the evolution of the morphology and the surface temperature of the flow at various dates;
- Results capture the relationship with topography and the partitioning of lava between the flow front, lateral breakouts and flow inflation.

Abstract

We present the evolution over 3 months of a 2016-2017 pāhoehoe flow at Kīlauea as it changed from a narrow sheet flow into a compound lava field fed by a stable system of tubes. The portion of the flow located on Kīlauea's coastal plain was characterized using helicopter-based visible and thermal structure-from-motion photogrammetry to construct a series of georeferenced digital surface models and thermal maps on 8 different days. Results reveal key influences on the emplacement and evolution of such long-lived pāhoehoe flows. This region of the flow grew by ~12×10^6 m^3 with a near-constant time-average discharge rate of 1.2-2.7 m^3/s. The development of two tube systems is captured and shows an initial nascent tube enhanced by a narrow topographic confinement, which later inflated and created a topographic inversion that

modulated the emplacement of a second flow lobe with its own tube system. The analysis of breakouts at various stages of the field's life suggests that the evolution of the thermal and morphological properties of the flow surface reflect its maturity. Thermal properties of breakouts were used to expand the empirical relationship of breakout cooling to longer time scales. This study contributes to the long-term development and the validation of more accurate predictive models for pāhoehoe, required during the management of long-lasting lava flow crises in Hawai'i and elsewhere.

1. Introduction

Pāhoehoe lava flows are the most abundant type of subaerial lava on the Earth's surface. They often form extensive, compound flow fields fed by complex, interconnected tube pathways formed during endogenous thickening via flow inflation (Macdonald 1953; Wentworth and Macdonald 1953; Walker 1991). Seminal studies such as Hon et al. (1994), Kauahikaua et al. (1998) and Self et al. (1998) have demonstrated that pāhoehoe growth is a complex balance between flow front advance, lateral breakouts behind the front and vertical inflation of the flow. As the flow inflates, a crust develops and insulates the flow, which progressively evolves into a molten core of interconnected pathways (Anderson et al. 1999, 2005, 2012; Schaefer and Kattenhorn 2004; Hoblitt et al. 2012; Orr et al. 2015). For this reason, pāhoehoe behavior is notoriously difficult to anticipate and forecast, especially when activity is widespread and focused within concealed, branching tube systems (Walker 1973). The location and dimensions of these tube pathways are controlled by complex and often local factors including topographic gradient, lava rheology, variations in supply rate (either at source or locally due to short-lived tube blockages) and the geometry of the feeder tubes themselves (Poland et al. 2016). These complex controls limit the development of accurate physical predictive models of pāhoehoe lava flows, the absence of which complicates hazard assessment and crisis management of long-lasting lava crises.

Over the past two decades, photogrammetry has been used in conjunction with other high-resolution imaging techniques to characterize the evolution of lava flows in four dimensions. Measurement techniques include stereo-imaging (James et al. 2007, 2010; James and Robson 2014) and structure-from-motion (SfM) photogrammetry from both manned and unmanned aerial vehicles (UAV; Farquharson et al. 2015; Turner et al. 2017b, a; Favalli et al. 2018) using a range of different sensors. Optical and light detection and ranging (lidar) sensors allow

construction of high-resolution surface models to analyse the evolution of morphological parameters that capture the dynamics of flow emplacement (James et al. 2009; Favalli et al. 2010; Behncke et al. 2016; Kolzenburg et al. 2016). Thermal mapping provides insight on the emplacement of new lava by showing its partitioning between various sectors of the flow field and help with inferring a cooling history (James et al. 2007; Harris et al. 2007; Patrick et al. 2017; Tarquini and Coppola 2018). These methods are usually applied separately, mostly on active ʻaʻā and open-channel flows and rarely at the scale of an entire flow. A recent study by Tarquini and Coppola (2018) demonstrated the range of insights that the combination of thermal and morphological characterizations could provide on a 2001 channelized ʻaʻā flow of Etna (Italy). However, a similar approach applied to long-lived, compound pahoehoe flows has never been attempted.

Lava flows from the East Rift Zone (ERZ) of Kīlauea volcano in Hawai'i have repeatedly impacted communities on the Island of Hawai'i, and more than 900 homes and other primary structures have been destroyed since 1983 (J. Babb, written communication, 2019). The assessment of the likely path and timing of inundation of pāhoehoe flows is a key challenge for hazard assessment and crisis management, but the complex interactions of physical and environmental parameters controlling the emplacement of pāhoehoe flows prevents the development of accurate numerical models. As a basis for interacting with stakeholders during crises, the Hawaiian Volcano Observatory (HVO) uses the 'path of steepest descent' method to create various scenarios for flow advance (Kauahikaua et al. 2017). Although this method has been used with success during various crises (Poland et al. 2016; Patrick et al. 2017; Turner et al. 2017b), new techniques of *in situ* measurement of the critical parameters controlling the emplacement of pāhoehoe must be developed to complement detailed but scarce field measurements (e.g. Chevrel et al. 2018) and inform complex and accurate predictive physical models (e.g. Kolzenburg et al. 2017).

We present here a reconstruction of the morphological and thermal evolution of a portion of a lava flow erupted from the Puʻu ʻŌʻō vent on the ERZ during 2016 and informally called the "episode 61g" flow (Orr et al. 2017; Patrick et al. 2019). Emplacement of the flow was captured from repeated helicopter flights over a period of over two months. Topographic models and orthomosaic images were constructed from both visible and thermal images using SfM photogrammetry. Combining visible and thermal sensors sheds light on the emplacement dynamics of a compound pāhoehoe flow as it evolved from a narrow flow dominated by a crust-free lava channel to a broad, stable, thermally-insulated tube-fed flow. This combined approach captures well the relationship between the pre-flow topography and the thermal and

morphological evolution of the flow. Results illustrate how the topographic changes induced by initial phases of the flow modulate the emplacement of later phases and capture the formation of a stable tube system through time. We first characterize the emplacement of the flow through time based on the thermal and morphological parameters, which are then used to discuss i) the interaction of pāhoehoe flows with the underlying topography, ii) the thermal and morphological evolution of breakouts through time, iii) the empirical cooling trends of surface breakouts and iv) the strengths and limitations of the path of steepest descent method for forecasting flow advance.

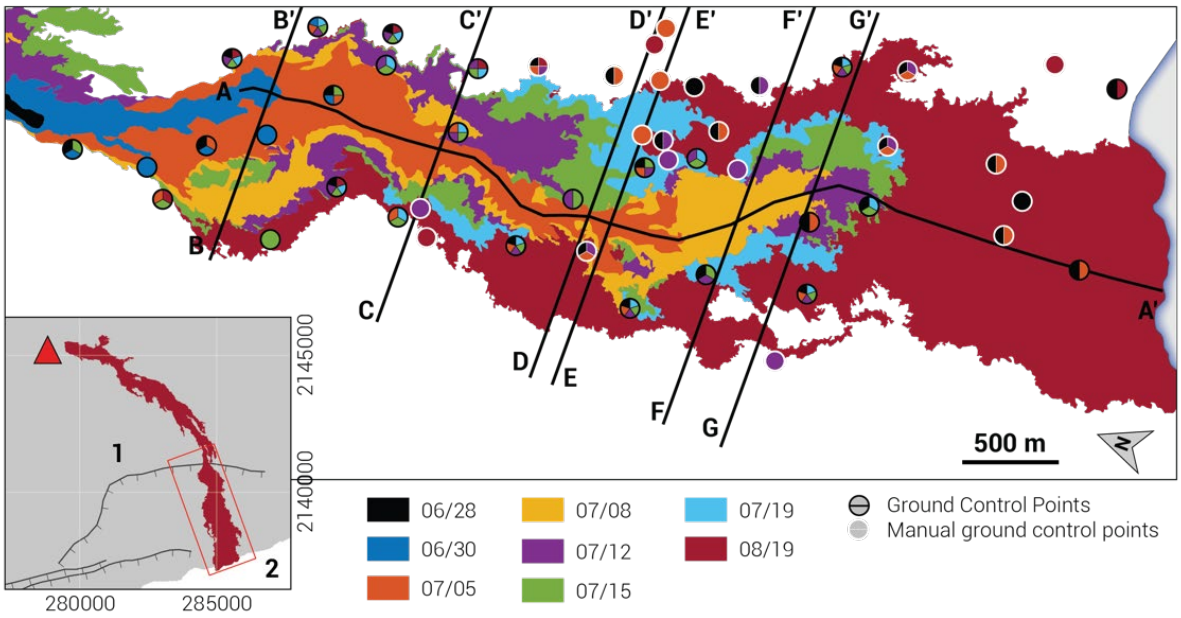

Figure 1: Maps of the study area. The inset map shows the outline of the 61g flow on August 19, 2016, extending from Pu‘u ‘Ō‘ō (red triangle), across the south flank of Kīlauea and down the Pūlama pali (1) and across the coastal plain to the Kamokuna ocean entry (2). The red rectangle delimitates the extent of the main map. The main map shows flow outlines (Orr et al. 2017) on the coastal plain for all dates, ground control points (GCP; circles with black borders) and manual GCP (i.e. natural features manually identified in multiple datasets and used as GCPs; circles with white borders). The colors of the ground control points correspond to the flow date(s) for which they were used. Black lines show the location of profiles used throughout the text.

2. Case-study: the 2016 episode 61g lava

Kīlauea’s 35-year-long Pu‘u ‘Ō‘ō eruption, which began in January 1983, was characterized much of the time by lava flows that traveled towards the south coast of the Island of Hawai‘i (e.g., Heliker et al., 2003, Orr et al., 2013). The episode 61g flow followed this pattern. It began erupting on May 24, 2016, on the east flank of Pu‘u ‘Ō‘ō at an elevation of 790 m. A second flow, episode 61f, started erupting almost simultaneously from the north flank of Pu‘u ‘Ō‘ō, but it stalled and became inactive by June 8, some 2 km from source.

Initially, the episode 61g flow advanced southeastwards at a rate of a few hundred meters per day (Fig. 1). By June 8, the episode 61g flow had captured all of the lava supply from Pu‘u ‘Ō‘ō, and a compound pāhoehoe flow began to develop. When the flow reached the top of the steep escarpment on the south flank of Kīlauea known as the Pūlama pali on June 28, it transitioned to an ‘a‘ā morphology. The Pūlama pali will hereafter be referred to as simply *the pali*. The channelized ‘a‘ā flow reached the base of the pali on June 30, and a new compound pāhoehoe flow began to develop on the coastal plain. This section of the flow initially advanced quickly as a narrow sheet flow at advance rates of up to 600 m/day, but it had slowed dramatically by July 5 and stalled in mid-July as lateral breakouts behind the flow front became active and the flow began to widen (Fig. 1). This initial flow front was overtaken by lateral breakouts during the third week of July, and the new flow front crossed the coastal road on July 25, entering the ocean on July 26 and forming a lava delta (the Kamokuna ocean entry; Fig. 1). Subsequent breakouts continued to widen the flow field and created a second ocean entry point and delta on August 9. The final flow length from the vent to the ocean entry is about 11 km.

Date (mm/dd)		**06/28**	**06/30**	**07/05**	**07/08**	**07/12**	**07/15**	**07/19**	**08/19**
Data availability									
DSM		✓ (n)	✓ (o)	✓ (n,o)	✕	✓ (o)	✓ (n)	✓ (o)	✓ (o)
Thermal		✓	✓	✓	✓	✓	✕	✓	✓
DSM georeferencing error from Pix4D Mapper									
μ (m)	**x**	0.01	0.01	-0.04	–	0.04	0.04	0.03	0.16
	y	0.01	-0.01	-0.01	–	-0.02	0-.05	0.03	-0.08
	z	-0.07	-0.01	-0.13	–	0.06	0.1	0 .02	-0.32
σ (m)	**x**	0.19	0.1	0.26	–	0.5	0.12	0.44	0.56
	y	0.18	0.06	0.19	–	0.19	0.21	0.39	0.74
	z	0.43	0.05	0.64	–	0.44	0.29	0.16	0.79
RMSE (m)	**x**	0.19	0.1	0.26	–	0.5	0.13	0.44	0.59
	y	0.18	0.06	0.19	–	0.19	0.21	0.39	0.75
	z	0.43	0.05	0.64	–	0.44	0.31	0.16	0.86
DSM precision analysis from James et al. (2017)									
Precision (m)	**z**	0.19	1.71	0.14	–	–	0.45	1.16	0.68
DSM co-registration error to 06/28									
$\mu_{\Delta z}$ (m)	**z**	–	-0.3	0.28	–	-0.12	-0.13	-0.52	-0.62
$\sigma_{\Delta z}$ (m)	**z**	–	0.69	0.89	–	1.23	0.95	1.96	1.14

Table 1: Availability and precision of all datasets. *Data availability* details the dates for which thermal maps and digital surface models (DSMs) were reconstructed (*n:* nadir; *o:* oblique). The *Georeferencing error* represents the alignment mismatch between measured and reconstructed GCP coordinates. The *Precision analysis* shows the average precision on the z coordinates assessed from the method of James et al. (2017) (see text for details on the averaging technique). Note that the precision could not be calculated for 07/12. The *co-registration error* represents a measure of elevation differences over a control area between a given date and the pre-flow topography (06/28). μ is the mean, σ is the standard deviation and *RMSE* is the root mean squared error.

3. Methods

3.1. Data acquisition

Datasets were acquired during eight helicopter overflights between June 28 and August 19, 2016. Note that i) the datasets are identified hereafter using their acquisition date expressed as mm/dd and, unless specified, all refer to the year 2016 and ii) the 08/19 dataset was acquired once the flow had already entered the ocean and no longer reflects the same emplacement regime compared to earlier dates. The primary objective of the overflights was the mapping and monitoring of the flow to inform stakeholders and the public. Consequently, flight plans were not explicitly designed for photogrammetric work, and image acquisition was generally opportunistic, although we benefited from experience gained during previous missions, including the use of a custom camera mount for nadir image acquisition. Visible and thermal datasets were simultaneously collected at altitudes of 200–600 m with a high variability in overlap and resolution due to sudden unanticipated changes in bearing and altitude.

Visible images were captured using both oblique and nadir approaches. For the former, pictures were taken manually from within the helicopter while attempting to optimize the overlap between successive shots and orienting the camera as steeply downward as possible. These images were acquired at high (>12 MP) resolution and with a maximum focal length of 35 mm using several cameras (Canon EOS 50D and 60D, Nikon D3300 and D7000). The reason for this camera variability was the rapidly scheduled context of the flights, which involved different science personnel, each using their own camera. For the nadir approach, a Canon EOS 50D was attached to the helicopter footstep using a custom mount. The camera shutter was triggered by a programmable intervalometer set at a frequency of either 0.5 or 1 Hz. The acquisition rate was set before takeoff and remained constant during the mission. The camera was not in an enclosure, so could not be used during poor weather.

Thermal images were acquired obliquely at 1 Hz using a handheld FLIR Systems SC620 camera with a 45° horizontal field of view and a resolution of 640 × 480 pixels. The medium gain

setting was used, which allows measurements from 0 to 550 °C (Patrick et al. 2017). Atmospheric attenuation was corrected following Patrick et al. (2017) using the FLIR *ThermaCam Researcher* software. By systematically assessing the sensitivity of the computed temperatures to external conditions (e.g. the ambient temperature and humidity, the acquisition distance and the emissivity value), Patrick et al. (2017) estimated a total uncertainty of about 6% on the final values. The reader is referred to the supplementary material of Patrick et al. (2017) for further details on the method.

3.2. Ground control points

30 ground control points (GCP) were set in the study area as the flow developed (Fig. 1). GCPs consisted of 1×1 m crosses of reflective material nailed to topographic high points on pre-existing lava surfaces. The location of the center of the cross was measured with a Leica System 500 kinematic GPS. Based on previous experience at HVO, this kinematic GPS provides a horizontal and vertical repeatability of 10-20 cm. Although we generally attempted to deploy GCPs the day before flights, this was not always possible. On early dates, GCPs were deployed as the flow advanced and there is a relatively low coverage on the coastal plain. On later dates, more GCPs were deployed on the coastal plain, but an increasing number of GCPs became overrun as the flow developed. GCPs were mostly located close to the flow edges, which are typically characterized by a lower point density in oblique-derived datasets. As a result, no single GCP is present across all dates, and datasets are variably well constrained (see Section 4.1).

3.3. Processing of visible images

Images were processed at their full resolutions using *Pix4D Mapper 3.2.14* and the resulting point clouds were geo-referenced using the GCPs in a WGS84 UTM 5N coordinate system. Because of the inconsistent GCP distributions between datasets, and to improve the co-registration of all datasets, natural features were manually identified in the 07/05 and 07/15 surveys and their photogrammetrically-derived coordinates were used as GCPs for georeferencing other datasets (manual GCP, mGCP; Fig. 2). Point clouds were densified by dense image matching within *Pix4D Mapper* and manually cleaned using *CloudCompare* to remove noise. Point clouds were then imported in *Matlab* to clip their extent to an area between the pali and the ocean entry (easting min/max: 284270/285950; northing min/max: 2137000/2140750) and to estimate an optimal grid resolution. Datasets were then imported in *ENVI* and interpolated to digital surface models (DSM). Since the area is mostly free of

vegetation, no filtering was performed and these DSMs are equivalent to digital elevation models (DEMs).

Precision analyses

Because of limitations introduced by the number and distribution of GCPs, our main concern here is to quantify the relative precision of the co-registration of the datasets, rather than the absolute overall geo-referencing accuracy. Three approaches were used to quantify this precision. First, *Pix4D Mapper* provides an estimate of the geo-referencing error from the differences between measured GCPs and coordinates estimated from photogrammetry. Because of the limited number of GCPs, none were used as check points. Second, the technique of James et al. (2017) estimates a 3D precision for all sparse points and gives insight into the spatial variability of precision across surveys. For this, *Pix4D Mapper* projects were imported into *Agisoft Photoscan Pro v1.2.6.* Some 2000 iterations of the Monte Carlo routines of James et al. (2017) were performed for each dataset and Z-precision maps were generated by averaging the elevation precision values for all points within a given cell size. Finally, the vertical co-registration error was estimated using the mean and the standard deviation of elevation differences between the DSM at a given date and the pre-flow topography within a control area. The control area is a region in which elevation should not have changed (i.e. no lava inundation) and was defined as a 50-m buffer around the flow at a given date. Following Favalli et al. (2010), the error on volume change was estimated using minimum (eq. 1) and maximum (eq. 2) errors:

(1) $Err_{V,low} = A\frac{\sigma_{\Delta z}}{\sqrt{N}}$

(2) $Err_{V,high} = A\sigma_{\Delta z}$

where A is the area of volume change, $\sigma_{\Delta z}$ is the standard deviation of height variations and N is the number of grid cells affected by volume change. These equations assume a constant error across the lateral extension of the flow and equally propagate the error $\sigma_{\Delta z}$ assessed at the flow edges over the entire dataset. In our case, the various limitations of the method applied to the episode 61g dataset (e.g., dominance of oblique SfM, variable acquisition altitudes) induce a poorer sampling density at the flow edges compared to the center. We therefore assume that equation 2 represents a maximum error.

3.4. Processing of thermal images

Thermal maps are routinely produced by HVO as part of the monitoring effort following the methodology of Patrick et al. (2015) and Patrick et al. (2017). Thermal images were processed

using *Agisoft PhotoScan Pro* to construct mosaics covering the flow extent. As described in Patrick et al. (2017), the resolution of the maps was generally around 1 m and were resampled to a consistent pixel size of 0.5 m. The mosaics were georeferenced on the flow outlines in *ArcMap* and imported in *Matlab* for analyses. For more information, the reader is referred to Patrick et al. (2017).

3.5. Flow properties

We used the flow outlines of Orr et al. (2017) to estimate flow length, area and width. Changes between successive DSMs were used to calculate the evolution of flow volume, with the 06/28 dataset used for the pre-emplacement topography. Following Patrick et al. (2017), new breakouts were identified using a threshold of 200 °C in thermal maps (equivalent to a surface <6 h old; Hon et al. 1994) and were classified as either lateral or surface breakouts using an arbitrary threshold of 100 m from the breakout centroid to the flow edge. We calculated the roughness of both the DSM and the thermal map for each breakout as the standard deviation of the residual of a best-fit plane fitted through all points within the breakout (Davenport et al. 2004).

4. Results

Outlines of Orr et al. (2017) (Fig. 1) are used to reconstruct the 2D evolution of the flow. Key properties are presented in Figure 2a-e, both as absolute values (left y-axis) and normalized per day (right y-axis). The flow initially developed in an elongation regime (i.e., time-averaged aspect ratio > 0; Fig. 2a, e) on the coastal plain as a narrow flow showing high advance rates and limited lateral expansion until 07/12 (Fig. 2a). Between 07/08 and 07/19, the flow advance rate decreased and episodes of breakout upslope on the east margin caused the flow to widen progressively (Fig. 2b,d). The flow reached the ocean entry on 07/26 and the area of the flow increased linearly between 07/19 and 08/19 (Fig. 2c).

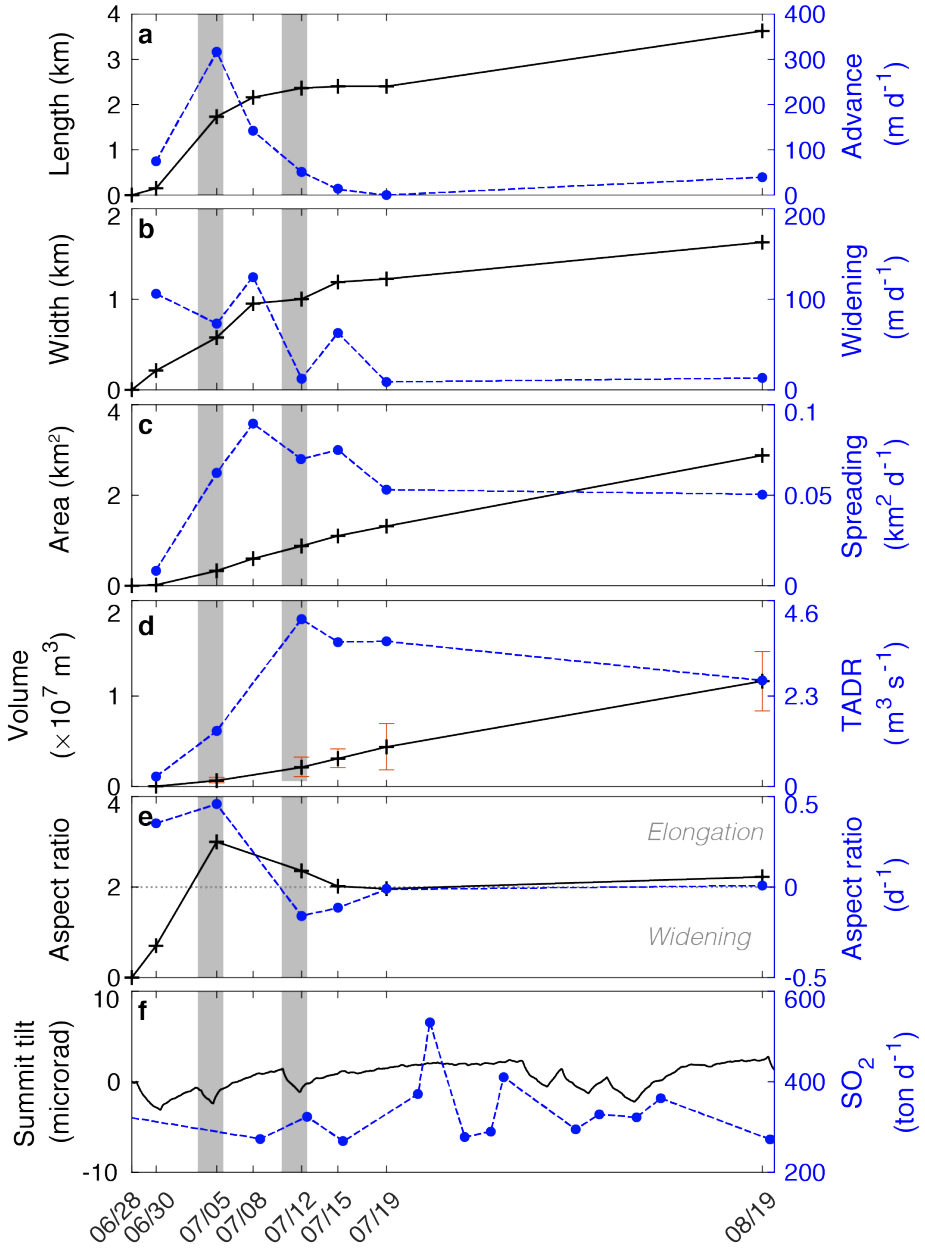

Figure 2: a-e Evolution of the properties of the 61g flow through time. Values are given by the left y-axes (solid black lines with crosses), with their associated rates on the right y-axis (dashed blue lines with dots). Note that for **a**, the length of the flow on 08/19 is a maximum length representing the distance to the ocean entry. For **d**, the error bars show the volume error estimated from equation 2. Note that the TADR on 08/19 does not account for the submarine part of the flow. Aspect ratio (**e**) is defined as the ratio between flow length and flow width. **f** Kīlauea summit tilt (left) and SO_2 flux (right) data are from the monitoring array of HVO. Shaded areas highlight deflation-inflation events that coincide with dates at which topographic and thermal datasets are available.

4.1. 3D reconstruction

Point clouds were reconstructed for all dates except 07/08, which was discarded due to the poor quality of the photogrammetry. Merging of nadir and oblique images was attempted to maximize flow coverage, but the combination of these two datasets sometime introduced large

alignment errors. As a result, two of the eight datasets were reconstructed using only nadir images, one was reconstructed using a combination of nadir and oblique images and four relied only on oblique images (Table 1). Thermal maps were available for all dates except 07/15, and flow outlines were available for all dates.

The precision analyses for all methods suggest decimetric uncertainties in 3 dimensions (Table 1). Note that i) only values within the flow outline were considered, except for 06/28, where no flow had developed yet in the region of interest, and ii) a precision analysis for 07/12 could not be created because of data loss. Results highlight that not all datasets are subject to the same precision. Most of the datasets have a mean geo-referencing error of ~10 cm and a root mean square (RMS) error of ~40 cm on the z component. Precision analysis following James et al. (2017) suggests that the 07/05 dataset has the best z precision (~10 cm), followed by 06/28 (~20 cm, except close to the ocean entry), 07/15 (~30 cm) and 08/19 (~70 cm), whereas 06/30 and 07/15 are characterized by meter-scale uncertainties. The vertical co-registration error to the pre-flow topography shows mean ($\mu_{\Delta z}$) and standard deviations ($\sigma_{\Delta z}$) varying between -0.62–0.28 and 0.69–2.0 m, respectively (Table 1).

Point clouds were interpolated into DSMs at a resolution that ensures that 95% of the pixels that were used contain ≥ 3 points (Whelley et al. 2014, 2017). Resolutions of 3, 5 and 9 m were tested. At a resolution of 3 m, only ~85% of DSM cells of datasets 07/12, 07/19 and 08/19 contained >= 3 points. At resolutions of 5 and 9 m resolution, only dataset 07/12 did not meet that criteria. Based on these observations, we chose the reasonable resolution of 5 × 5 m whilst recognizing that the 07/12 DSM will be more prone to interpolation errors.

Date	**Volume ($x10^6$ m^3)**	**Error ($x10^6$ m^3)**	
	Cumulative	**Minimum**	**Maximum**
06/30	0.04	0	0.012
07/05	0.66	0.003	0.292
07/12	2.14	0.006	1.078
07/15	3.1	0.005	1.043
07/19	4.38	0.011	2.572
08/19	11.65	0.01	3.296

Table 2: Cumulative bulk volumes of the 61g flow within the study area. The minimum and maximum errors are given by equations 1 and 2, respectively (see text for more detail).

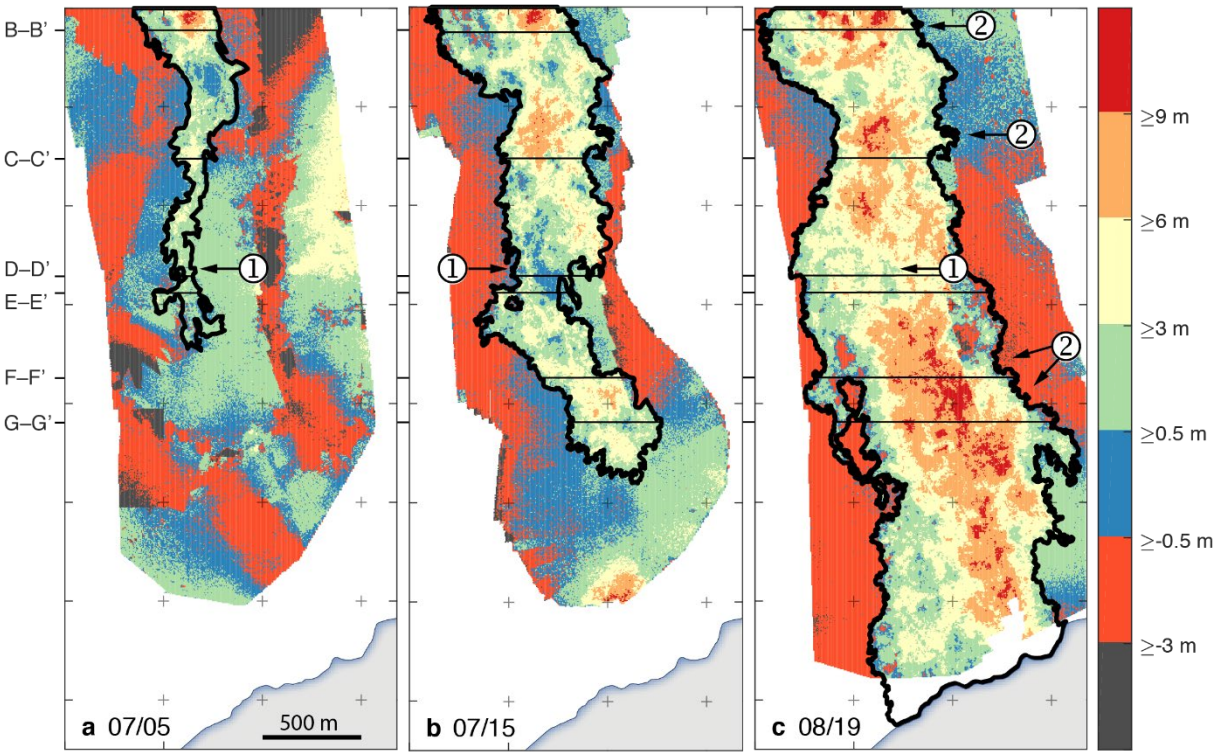

Figure 3: Elevation changes calculated as the difference of the DSM between 06/28 and **a** 07/05, **b** 07/15 and **c** 08/19. Flow outline for each date is shown in black. Grid intervals are 500 m starting from the northernmost edge. Numerical labels indicate 1: the region of limited thickness growth and 2: the regions of maximum final thickness discussed in the text. Cross-sections used in the text are shown as black lines and labeled on the left of the figure.

4.2. Evolution of the flow field

4.2.1. Topographic evolution

Elevation differences between sequential DSMs (Fig. 3) show how the initial channelized phase of the flow (~1,250 m down-flow; section D-D' on Fig. 1), evolves as one of the regions with the least volume change. Three main regions of maximum elevation change can be identified: i) north of the study area at the break-in-slope at the base of the pali, ii) between 500-1,000 m down-flow and iii) from 1,500 m down-flow to the ocean entry (Fig. 3c). Note that the two latter maxima are located just up- and down-flow of the smallest elevation change corresponding to the initially narrow part of the flow.

Volumes of the flow within the study area are summarized in Table 2 and show a value on 08/19 varying between $11.65 \pm 0.01 \times 10^6$ m^3 (eq. 1) and $11.65 \pm 3.2 \times 10^6$ m^3 (eq. 2). Figure 2d shows the evolution of the volume derived from DSM differences. The cumulative volume change was calculated as the difference from the baseline DSM and increases at a relatively steady rate.

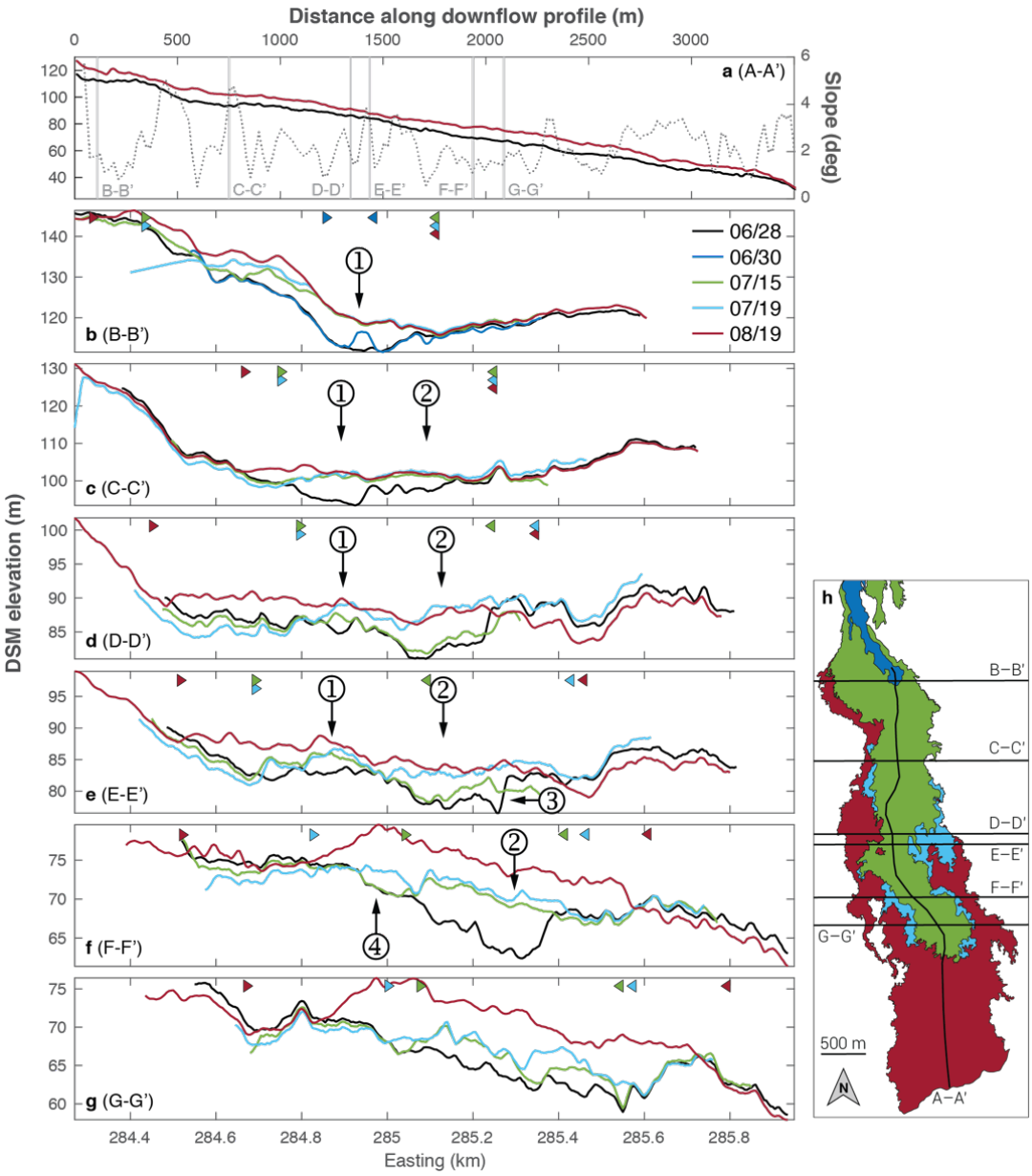

Figure 4: Elevation profiles for sections defined in Fig. 1. **a** Downflow profiles for 06/28 (black line) and 08/19 (red line). The dotted grey line shows the slope calculated from 06/28 and shown using a moving average with a window of 20 m. **b-g** Crossflow profiles. **h** Location of the profiles for the selected flow dates. Leftward and rightward pointing arrows represent the eastern and western edges of the flow, respectively, at a given date extracted from the flow outlines of Orr et al. (2017). Numerical labels indicate: 1-2, the down-flow evolution of the two main topographic confinements; 3, artifact in the reconstruction of the dataset 06/28 (see text for further details) and 4: self-created topographic feature.

The time-averaged discharge rate (TADR) gradually increases between 06/30 and 07/12, though it mostly ranges between 1–4×10^5 m^3/day (Fig. 2d). By 08/19, the reduction of TADR is most likely due to the presence of the ocean entry, which creates a pathway through which fresh lava is directly transported to the ocean without causing a volume change on land. A constant TADR in the study area was estimated by fitting the cumulative volume with a linear equation (Fig. 2d, Table 2), resulting in a mean TADR of 2.4×10^5 m^3/day or 2.8 m^3/s. Chevrel et al. (2018) measured a vesicularity of the 61g lava of about ~50% on breakouts that occurred

in November 2016 on the northern part of our study area. Using this value to estimate a dense rock equivalent (DRE) and the most conservative formulation of error (i.e. eq. 2) suggest a DRE TADR of 1.0 m^3/s. Values from other flows from Pu‘u ‘Ō‘ō (e.g. 40%, Orr et al. 2015; 25%, Poland 2014) increase the DRE TADR to 1.2-2.7 m^3/s. Although these values are only based on the most distal 3.5 km of the flow, thermal images of the entire flow show that our study area captures most surface activity from 07/12 on. These values of DRE TADR are similar to previously published mean values for the 2010-2016 eruptive period of Pu‘u ‘Ō‘ō (e.g., ~1 m^3/s for late 2010, Orr et al. 2015; 1.5 m^3/s for 2011-2012, Poland 2014; 1.3 m^3/s for 2014-2016, Patrick et al. 2017) but are lower than the Pu‘u ‘Ō‘ō’s long term effusion rate of ~4 m^3/s for the period 1983–2002 (Sutton et al. 2003) and the 2018 lower Puna eruption (>100 m^3/s).

Previous studies have linked the inflation phase of deflation-inflation events to lava surges and pressurization of tube systems (Orr, 2011; Anderson et al., 2015; Orr et al., 2015; Patrick et al., 2017). Two deflation-inflation events appear to coincide with flow widening (shaded bands in Fig. 2), but the absence of DSM and thermal maps between these events prevents identifying their direct effects on the TADR (Fig. 2f). No significant change in SO_2 emissions is identifiable during the periods for which DSM and thermal data are available (Fig. 2f).

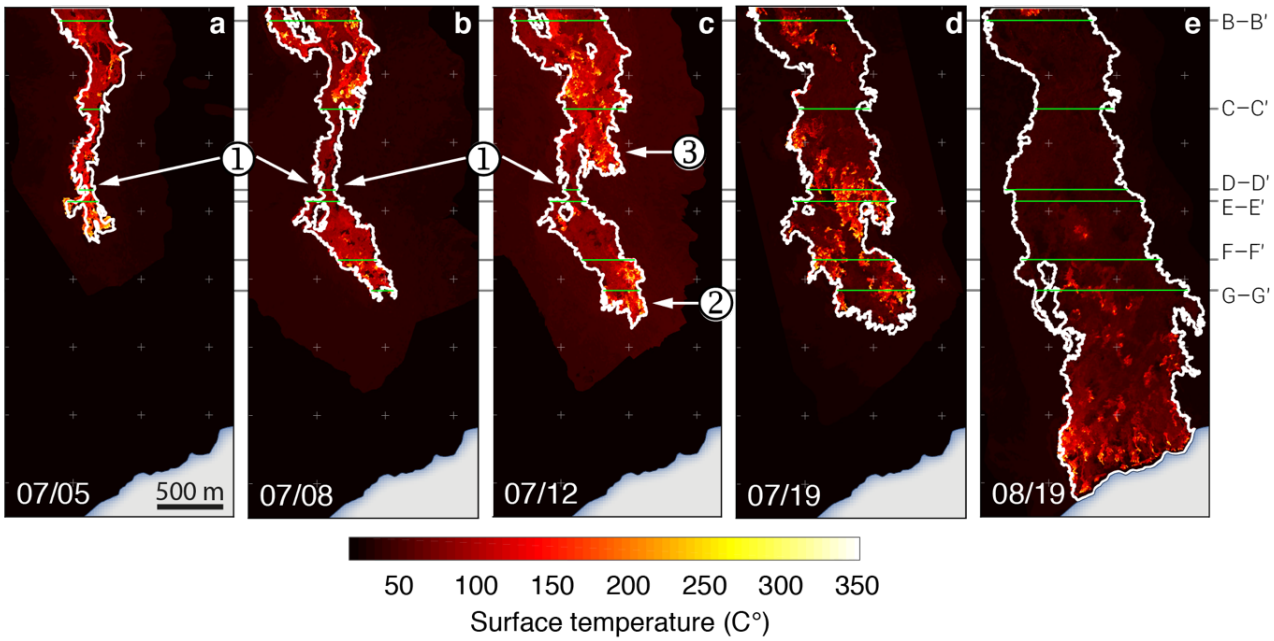

Figure 5: Thermal evolution of the 61g flow. White lines are flow outlines. Grid intervals are 500 m. Numerical labels indicate 1: the initial narrow region of the flow, 2: evidences of mass transfer through the narrow section of the flow and 3: surface activity widening the flow. Cross-sections used in the text are shown as green lines and labeled on the right of the figure.

364 *4.2.2. Pre-flow topography*

365 Down-flow (Fig. 4a) and cross-flow profiles (Fig. 4b-g) of DSMs show, that in most cases,
366 alignment mismatch between datasets gradually increases laterally beyond the flow edges, but
367 small features are consistently captured within the flow outlines. North to south along the axis
368 of the flow, the first 350 m of pre-flow topography is dominated by the break in slope between
369 the pali and the adjacent flat area (Fig. 4a). This flat area, with a slope constantly <2°, is
370 followed by two slightly steeper regions (up to ~5°; 400 and 750 m down-flow). The remaining
371 portion of the flow has an average slope of ~2° with local maxima up to ~4°.
372 Cross sections (Fig. 4b-g) show a topographic confinement exists at the base of the pali (feature
373 1; Fig. 4). This extends for 1,500 m down-flow to section E-E', where it ends abruptly (Fig.
374 4e). By section C-C', a relatively flat surface extends east of the initial topographic confinement
375 (feature 2 in Fig. 4c-f) and evolves down-flow into a wide, asymmetric valley traceable down
376 to the ocean entry. Note that a reconstruction artifact corresponding to a region of very low
377 point density on the point cloud is visible on the pre-flow topography (feature 3 in Fig. 4e).
378

379 *4.2.3. Thermal evolution*

380 The thermal map on 07/05 shows a uniform and relatively high temperature distribution across
381 an initial narrow flow fed by open channels on the pali (Fig. 5a). Between 07/05 and 07/12 (Fig.
382 5a-c), the narrow part of the initial flow cooled significantly, which suggests the development
383 of a stable crust. The flow front advance almost stalled between 07/08 and 07/12, but local
384 breakouts and high temperatures at the flow front suggests that fresh lava was still supplied
385 through the narrow section of the flow (Fig. 5c). By 07/12, lateral breakouts north of the narrow
386 section initiated an eastward widening of the flow. Between 07/12 and 07/19, the overall surface
387 temperature on the north part of the flow decreased from >150 °C to <100 °C. Simultaneously,
388 patterns of surface activity on the south part of the flow changed from wide, smooth and
389 relatively uniform high temperatures to localized, rougher, more irregular areas of high
390 temperatures surrounded by significantly cooler temperatures. By 08/19, except for occasional
391 breakouts at the base of the pali, most of the surface activity was located on the south part of
392 the flow as localized breakouts (Fig. 5e).
393

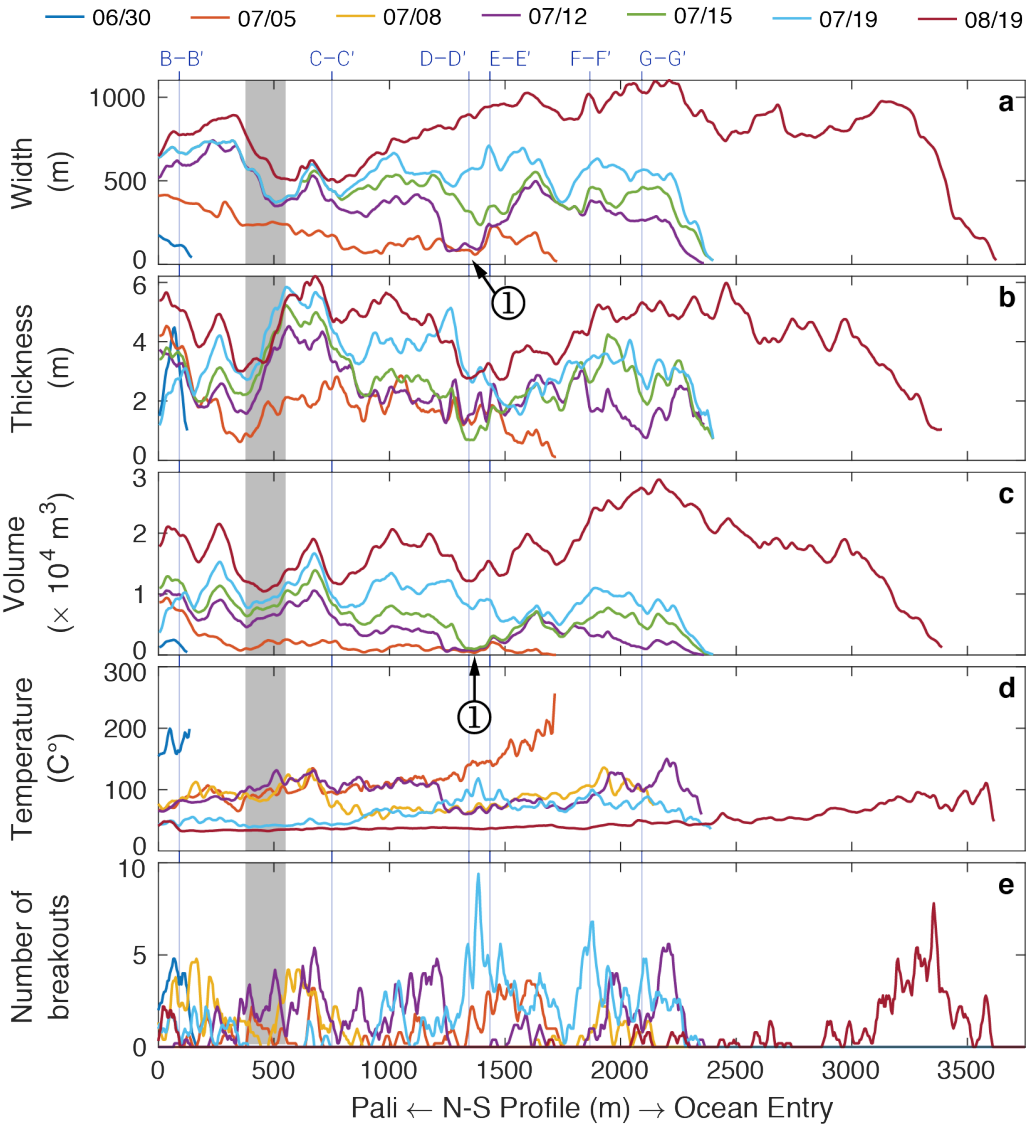

Figure 6: Downslope evolution of the properties of the 61g flow for selected dates. For each downslope increment of 5 m, the properties of the pixels contained within the flow outline are averaged. **a** flow width based on the flow outlines of Orr et al. (2017); **b-c** thickness (b) and lava volume (c) using the difference in DSMs between a given date and the baseline (06/28); **d** mean temperature and **e** number of breakouts. The shaded area shows the region of maximum slopes observed in Fig. 4. Label 1 indicates the expression of the narrow section of the flow (feature 1 of Figs. 3, 4 and 5). Vertical blue lines show the location of cross-sections (Fig. 4).

4.2.4. Downflow evolution of flow properties

Down-flow properties are calculated either by an integration (volume), a mean (thickness and temperature) or a sum (breakouts) across E-W cross-sections moving down flow with a window width of 5 m (Fig. 6). Regions with high slopes consistently show reduced flow width and thickness. The initial narrow flow described in Section 4.2 is expressed on Figure 6 (feature 1). Between 07/05 and 07/08, it retained constant width and thickness (Fig. 6a, c) during rapid cooling (Fig. 6d). Simultaneously, the volume of lava, both up-slope and down-slope of this narrow section, increased by widening and thickening.

Surface temperature of early datasets capture both the highest temperatures and the smallest number of breakouts. The evolution of the surface temperature records the downslope propagation of progressive insulation of the flow surface and reflects an increasing flow maturity (Fig. 5, Fig. 6d).

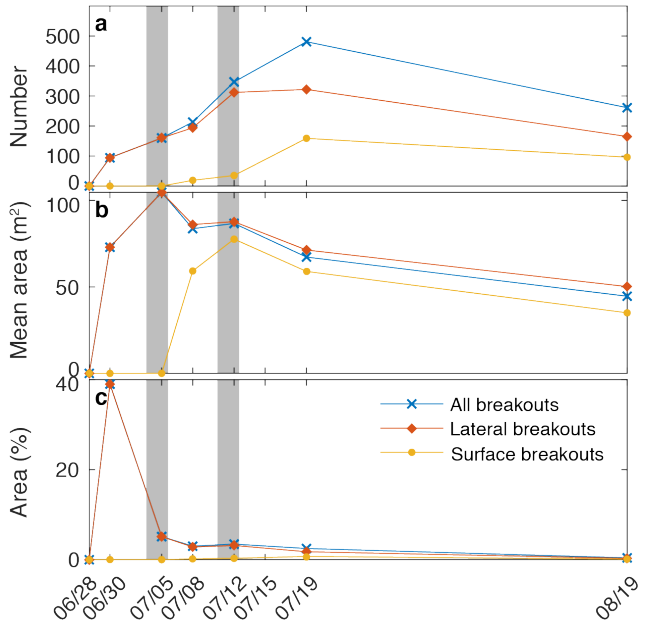

Figure 7: Evolution of active breakout properties through time in terms of total number of breakouts, mean breakout area and the total area covered by breakouts. Distances from the flow edge are the distance between the center of the breakout centroid and the flow outlines of Orr et al. (2017). Shaded areas indicate episodes of deflation-inflation events identified from Fig. 2.

4.2.5. Patterns of surface activity

Due to our definition of lateral breakouts based on a distance from the flow margin, the early, narrow initial flow is characterized by a relatively small amount of large lateral breakouts until 07/05, when a deflation-inflation event occurred and the flow started widening (Fig. 7, Fig. 5b). 07/12 marks the onset of surface breakouts and corresponds to both significant flow widening and then to the inflationary phase of a second deflation-inflation event. From 07/19, both the number and area of breakouts decrease, which agrees with the apparent surface cooling trend of the northern portion of the flow (Fig. 5d,e; Fig. 6d,e). Except for 06/30, the total breakout area represents 2-5% of the flow area until 07/19, after which it drops to <1%. Lateral breakouts are consistently larger than surface breakouts (Fig. 7b).

5. Interpretation

The initial development of the episode 61g flow on the coastal plain (06/30-07/08) is interpreted as the establishment of a tube system enhanced by topographic confinement. The narrow flow

433 on 07/05 was controlled by a topographic valley whose cross-sectional area decreased between
434 sections B-B' and D-D' (feature 1 in Fig. 4). Between 07/05 and 07/08, a 750 m-long region
435 cooled whilst showing no lateral expansion and limited vertical inflation (feature 1 in Fig. 5).
436 Advance and widening of the flow south of section D-D' provide evidence that material was
437 still transported to the flow front, thus suggesting that a tube was present.
438 By 07/08, new 'a'ā flows appeared on the pali (Fig. 5b), probably caused by a lava surge within
439 the system related to the inflation phase of a DI event. Increasing topographic confinement
440 between sections C-C' and D-D' (Fig. 4c, d) did not allow expansion to accommodate the
441 hydraulic pressure caused by the increase in discharge. Consequently, intense surface activity
442 occurred north of the tube and breakouts started flooding the secondary topographic low east
443 of the initial flow path (feature 2 on Fig. 4), causing an eastward branching. Between 07/12 and
444 07/19, the flow widened and thickened but barely advanced.
445 The flow reached the ocean on 07/26. Despite a paucity of data, cross sections between 07/12
446 and 08/19 suggest that thickness increases above the east topographic low (feature 2 on Fig. 4)
447 might be related to the development of a second tube branch. This branch appears as a
448 conspicuous north-south lineament of maximum thickness change on the east margin of the
449 flow (Fig. 3c). On 08/19, the lower 2000 m of the flow field show a thick flow (≥6 m, locally
450 ≥9 m; Fig. 6) with an axis located above the main thalweg of the topographic valley (Fig. 3c).
451 Between 07/19 and 08/19, the flow also widened westwards between 1,500 and 3,000 m from
452 the pali (Fig. 5; sections B-B' to D-D', Fig. 4), creating the region of the flow with the smallest
453 thickness change (Fig. 3). This event is first visible on section B-B' (Fig. 4b) along the west
454 side of the flow and is traceable on section C-C' (Fig. 4c) as a filling of a topographic low west
455 of feature 1. By section D-D', this new portion of the flow clearly becomes isolated from the
456 central flow by a topographic high that divided the flow (feature 1 on 07/19, Fig. 4d). This
457 branch of the flow is still visible on section E-E' (Fig. 4e) but no longer appears by section F-
458 F' (Fig. 4f).
459
460

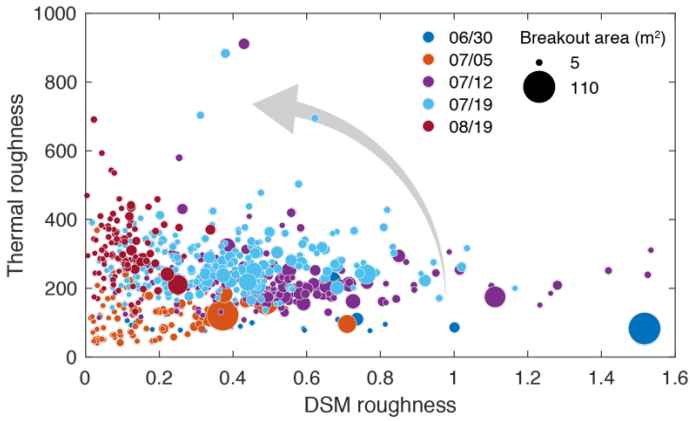

Figure 8: The thermal and elevation roughness of all breakouts. The symbol diameter is scaled to the breakout area. The grey arrow shows the maturing trend from an early low thermal roughness / high terrain roughness field to a more mature high thermal roughness / low terrain roughness field.

6. Discussion

6.1. Breakout characteristics

The surface morphology of pāhoehoe flows is a consequence of the combined effects of effusion rates, cooling rates and the underlying topography (Katz and Cashman 2003; Gregg and Keszthelyi 2004; Rader et al. 2017; Gregg 2017; Rumpf et al. 2018). Hon et al. (1994) introduced two breakout morphologies. Sheet breakouts are single broad units characterized by abrupt margins, smooth surfaces and temperatures decreasing from the front of the breakout that correspond to an increase of the crust age. Such breakouts are observable on early datasets (e.g. 07/05; Fig. 5a). Alternatively, hummocky breakouts consist of multiple breakouts scattered over the flow surface with variable temperatures and are clearly observable on 08/19 (Fig. 5e), weeks after the episode 61g flow had reached the ocean. Studies by Patrick et al., (2017) and Turner et al., (2017b) suggest that the type of breakout is controlled by the maturity of the flow field and supply rate to the system, which is supported by lab experiments and previous observations (Gregg and Keszthelyi 2004; Tarquini and de' Michieli Vitturi 2014; Rader et al. 2017).

Sheet flows occurred on dates characterized by relatively high advance rates and aspect ratios (e.g. 07/05; Fig. 2a, b). They show high temperatures at the flow front and are significantly less numerous than later hummocky fields (Fig. 6). Hummocky textures become evident on thermal maps from 07/19, by which date the northern part of the flow significantly cooled (Fig. 5d). By then, the east lobe of the flow, resulting from the presumed constriction of the tube described previously, is characterized by surface breakouts and irregular thermal textures. This breakout

field is easily recognizable between 1,250 and 1,750 m on Figure 6d-e and shows a higher mean temperature and number of breakouts.

Characterizing each breakout as a function of its topographic versus thermal roughness suggests an evolution corresponding with the maturity of the flow surface (Fig. 8). Immature surfaces, characterized by a thinner crust, inflation regimes and sheet breakouts, plot in a high topographic roughness/low thermal roughness field, and the topographic roughness of sheet breakouts increases with area. This relates to both the narrow nature of the flow on early dates that covered the area with the most important changes in slope and by methods for roughness calculations that do not allow gradient effects to be eliminated. As the flow evolves and becomes more mature, with a thicker crust and the development of an ever-more-stable tube system, the development of hummocky breakouts shifts this trend towards a low topographic roughness/high thermal roughness field. This pattern is attributed to the smaller and less sustained lava supply to an individual breakout that will cause lava to fill lows between preexisting hummocky topography and rapidly form stable crust. Although this trend (Fig. 8) only captures the surface expression of morphological changes without considering controlling mechanisms, it potentially provides a method to characterize the relative influence of external variables (e.g. supply rate, underlying topography) acting during the evolution of a pāhoehoe surface.

The approach outlined here requires a resolution of both thermal and DSM time series to scale the size of the targeted feature. Pāhoehoe flows ideally require high temporal and spatial resolutions to capture small and rapidly evolving features such as breakouts at toes scales. However, instruments with coarser resolutions (e.g. Tan-DEM-X, Sentinel, SEVIRI) might be able to capture evolving regions of silica-rich flows (e.g. inflation; Kolzenburg et al. 2018) occurring at larger spatial scales over longer time periods. This could have implications for the monitoring of remote areas (e.g. Kamchatka, Aleutians).

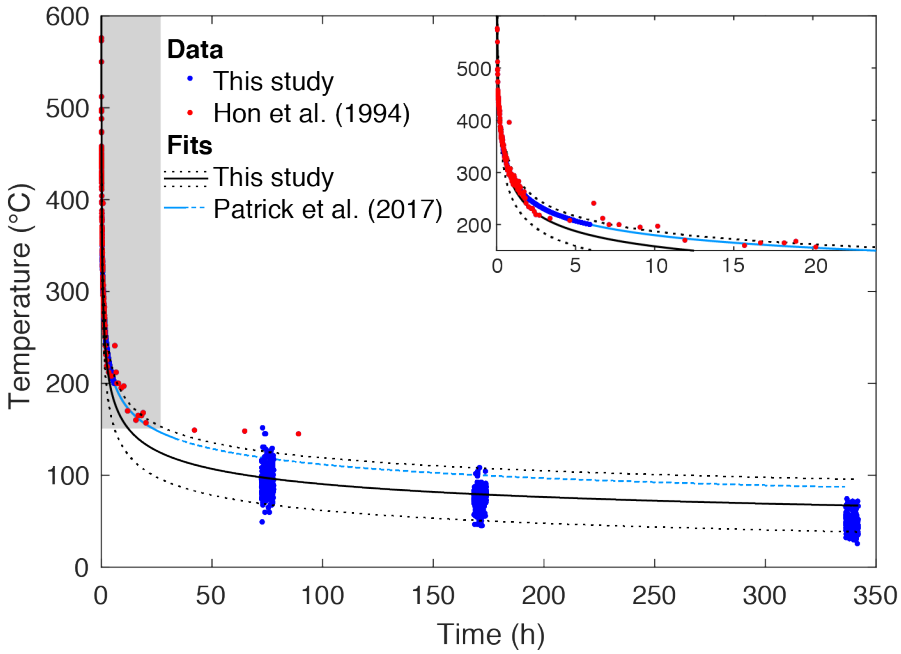

Figure 9: Empirical power law cooling relationships fitted to thermal data of the 61g flow (blue dots) combined with the surface data of Hon et al. (1994) (red dots). The blue curve shows the fit of Hon et al. (1994) modified by Patrick et al. (2017) ($T_{surf} = 288.65t^{-0.2060}$; dashed after 33 h). The black curve shows the power law fit with the 90% confidence interval shown as dotted lines ($T_{surf} = 277.04t^{-0.2438}$). The gray box shows the region of the inset plot, which is zoomed to a maximum time of 24 h.

6.2. Cooling trends

Previous studies of pāhoehoe flows at Pu‘u ‘Ō‘ō have proposed that the surface of breakouts develops a viscoelastic crust below a temperature of ~1,070 °C, and a brittle crust below ~800 °C (Hon et al. 1994; Self et al. 1998). Hon et al. (1994) described the surface cooling below a temperature of 1,070 °C within the first 100 h with an empirical logarithmic function:

$$T_{surf} = 140 \times \log(t) + 303 \quad (3)$$

where T_{surf} (°C) is the surface temperature and t is the time (h). Harris et al. (2007) used this relationship to estimate the age of a lava crust from surface temperature in thermal images, while restricting the validity of this relationship to a maximum age of 48 h. With a similar purpose, Patrick et al. (2017) found that the original data of Hon et al. (1994) were better described by a power law and restricted its validity to a maximum age of 33 h:

$$T_{surf} = 288.65 \times t^{-0.2060}. \quad (4)$$

Here, we use the thermal maps of the episode 61g flow to explore the cooling trend of long-lived pāhoehoe fields at Pu‘u ‘Ō‘ō over a longer period by applying the following workflow. Ages of all pixels with a temperature >200 °C on 07/05 were calculated using equation 4 and

their subsequent thermal histories were retrieved in datasets 07/08, 07/12 and 07/19 (Fig. 9). For later dates, the time is the elapsed time between flights. Note that i) the 08/19 dataset was ignored because of the month-long data gap with 07/19, and ii) to obtain cooling unaffected by subsequent breakouts, only pixels showing a decreasing trend of temperature between 07/05 and 07/19 were preserved. This dataset was combined with the surface data of Hon et al. (1994). Fitting a power law of the shape $y = ax^b$ suggests a = 277.50 (90% confidence interval between 276.38 and 278.62) and b = -0.2438 (90% confidence interval between -0.2455 and -0.2421). Compared to the relationship of Patrick et al. (2017), this new relationship generally underestimates the cooling rate of Hon et al. (1994). Despite a discrepancy with the cooling rates of Hon et al. (1994) and Patrick et al. (2017), this approach can nevertheless provide an empirical insight to the long-term cooling trend of compound pāhoehoe flows when time series of thermal images are available.

6.3. Tube system

The interpretation of two branches to the tube system, based on flow outlines, DSMs and thermal maps matches observations in the field (Fig. 10a). The earlier branch, located west of the flow, follows the outline of the initial flow front and confirms our interpretation that its development was promoted by a topographic feature. Limited variations in width, thickness and temperature suggests that the initial sheet flow developed a crust and underwent little inflation (e.g. Calvari and Pinkerton, 1999; Hon et al., 2003; Peterson and Swanson, 1974; Peterson and Tilling, 1980). The second branch resulted from the eastward widening of the flow that utilized the valley visible on the pre-flow topography. Its path follows the shape of the flow front on 07/15 and provides an additional illustration of how the emplacement of later parts of compound flows are influenced by topographic features created by earlier parts.

6.4. Relationship with topography

The emplacement of pāhoehoe flows is influenced by both small and large scale properties of the underlying topography (Hon et al. 1994; Fujita et al. 2009; Scifoni et al. 2010; Dietterich et al. 2015; Rumpf et al. 2018). At a breakout scale, Hamilton et al. (2013) estimate that topographic obstacles that are greater than ~15% of the toe's initial thickness may significantly affect the flow emplacement. At a larger scale, high gradients (>~10°) induce a change in the flow morphology similar to an increase in supply rate (Gregg and Fink 2000), whereas changes from steep to flat slopes promote heat dissipation and induce thicker flows (Glaze et al. 2014;

Tarquini and Coppola 2018). In the region of slope >4° (Fig. 5a), the inertia gained on steeper slopes promotes transportation over deposition and results in a region of minimum final thickness (Fig. 3, Fig. 6; e.g. de' Michieli Vitturi and Tarquini, 2018; Dietterich and Cashman, 2014).

Pāhoehoe flows alter local topography and, through inflation, induce topographic inversions (Hamilton et al., 2013; Hon et al., 1994; Self et al., 1998; Turner et al., 2017; Walker, 1991). This process is clearly visible in our dataset (e.g. features 1 and 4 on Fig. 4). These self-formed positive topographic features can modulate subsequent developments of compound flows. This is illustrated by the westwards widening that occurred between 07/19 and 08/19 (Fig. 1), which was conditioned by a separating feature resulting from the inflation of the initial narrow flow emplaced on 07/05 (feature 1 in Fig. 4). It is worth noting that recent observations have highlighted a similar behaviour of dominantly 'a'ā flows (Kolzenburg et al. 2018).

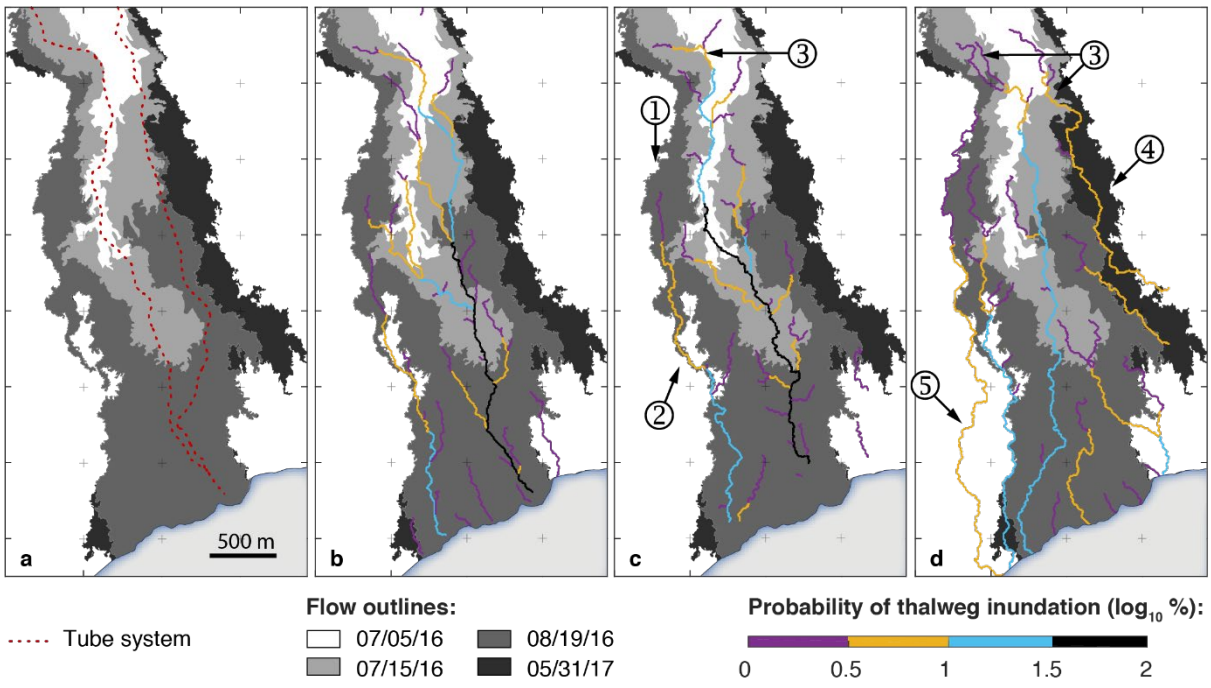

Figure 10: a Tube system mapped in the field by the HVO staff; **b-d** paths of steepest descents produced using **b** the HVO DEM (see text for details), **c** the 06/28 DSM and **d** the 08/19 DSM. **b-c** using the method described in the text using DSMs produced for **c** 06/28 and **d** 08/19. Grid intervals are 500 m.

6.5. Comparison with the steepest descent approach

The path of steepest descent method is used by HVO during crises to derive various scenarios of lava inundation (Kauahikaua et al. 2017). Since this method relies uniquely on elevation

models, we test here its sensitivity to topographic models acquired from different sources and at different stages of the emplacement of long-lived compound flows. We first compare the 4.5 m resolution DEM used by HVO to forecast flow direction on the coastal plain, which is a combination of the bare-earth USGS DEM and the 2013 Tandem-X InSAR data (M. Poland, personal communication, hereafter referred to as HVO DEM), with our DSM on 06/28. We then compare DSMs obtained on 06/28 and 08/19. For each date, 10,000 random points were sampled over the 08/19 flow footprint and their paths of steepest descent were computed in *Matlab*. Results express the probability of inundation of a thalweg by normalizing the frequency of inundation of a given pixel by the total number of simulated points (Fig. 10).

Although both pre-topography terrain models succeed in forecasting flow directions within the 08/19 flow outline, subtle differences suggest that the 06/28 DSM (Fig. 10 c) outperforms the HVO DEM (Fig. 10 b). First, the main path obtained from the 06/28 DSM captures the sinuosity of the initial phase of the flow until at least 07/15. Conversely, the HVO DEM results in a main path located east of the observed flow, which corresponds to the secondary topographic low observed in Figure 4. Second, paths obtained with the HVO DEM require the flow to migrate through 3 different lavasheds to reproduce the inundation path observed on 07/05, whereas a single one is required when using the 06/28 DSM. Finally, the west branch observed between 07/19 and 08/19 cannot be described by the drainage obtained by the HVO DEM. On the contrary, the 06/28 resolves the source drainage and precisely describes the path of inundation.

Results obtained with the 06/28 and the 08/19 DSMs outline the evolution of the drainage pattern as the flow develops. Using the 06/28 DSM, topographic confinement down the pali (Fig. 4) results in one main inundation path joined by tributaries ~250 m and ~750 m downflow (Fig. 10 c). These two junctions correspond to two northernmost areas of maximum vertical changes on 08/19 (Fig. 3c), which divided the initial drainage pattern into two distinct branches (Fig. 10 d). The drainage pattern from the 08/19 DSM explains the eastward widening of the flow between 08/19/16 and 05/31/17, which follows a path of inundation not accounted for by the 06/28 DSM. These observations highlight how quickly the surface of pāhoehoe flows evolved topographically through time and demonstrate the need to rapidly update DSMs during crises.

This sensitivity analysis confirms the importance of the topographic model (Turner et al. 2017). The regular update of both DSMs and maps of paths of steepest descent can provide insights

on the temporal evolution of the hazard of long-lasting pāhoehoe lava flows which, in combination with thermal maps, represent an improvement to the traditional use of the steepest descent approach. Although this prediction estimate does not account for critical elements of hazard assessments (e.g. temporal components, uncertainties, probabilities to exceed critical hazard thresholds), it is a pragmatic alternative to a rigorous forecast relying on models that cannot incorporate such complex processes as breakouts, inflation, thermal insulation or tube formation. In this context, combined visible and thermal SfM collected during routine monitoring provide insights on both the emplacement mechanism and potential patterns of future inundation.

7. Conclusions

The application of SfM photogrammetry techniques to visible and thermal datasets provides unprecedented detail in characterizing the emplacement of a compound pāhoehoe lava flow. Only the combination of these two data types fully captures the dynamic nature of the factors, interactions and feedbacks modulating the evolution of long-lived pāhoehoe fields. Regarding the studied portion of the 61 g lava flows, this study shows how:

- ~$12x10^6$ m^3 of lava accumulated on the flood plain over ~2.5 months, which corresponds to a DRE TADR of 1.2-2.7 m^3/s. This is similar to other measurements for the 2010–2016 period and about half that of the long-term effusion rate for the Pu‘u ‘Ō‘ō eruption;
- The flow developed over the first 1.5 km of the coastal plain under a dominantly elongating regime as a crust-free sheet flow that was fed by ‘a‘ā channels down the pali. The flow front then stalled, and a new pulse of lava caused the flow to widen. On 07/23, the flow reached the ocean entry and the pressure drop in the system resulted in little change in the flow morphology;
- Two main branches to a tube system developed, the first was enhanced by a narrow confinement that caused a topographic inversion via inflation, conditioning the emplacement of the second branch;
- The initial confined branch of the tube system may have acted as a bottleneck during an episode of lava surge, thus increasing the fluid pressure up-flow and triggering lateral breakouts and flow widening.

Results also yield wider implications for the understanding of long-lived compound pāhoehoe flows, their forecasting and the management of associated crises. Key findings include:

- The ability of SfM-derived DSMs to capture critical small-scale features required for the accurate forecast of the flow path;
- The breadth of information that the combined use of DSMs and thermal maps at successive time intervals can supply for the dynamic of emplacement of a pāhoehoe flow, from which subjective interpretations can inform short-term scenarios of inundation;
- A proposed extension of the cooling trend of breakouts of Hon et al. (1994) to longer time frames. Although our relationship requires further research to be applied operationally, it nevertheless demonstrates how successive thermal maps could support an empirical characterization of physical process as a basis for numerical models;
- A trend for the evolution of thermal and morphological properties of breakouts with time, which appears to describe the maturity of the flow field;
- An enhanced capacity of the method of steepest descent to accurately inform inundation path if combined with updated DSMs.

Although we recognize that the time required to process, geo-reference and analyze SfM data might hinder its application in an operational context during crises, the methodology developed here has demonstrated potential to characterize thoroughly the dynamics of emplacement of long-lived compound pāhoehoe flows.

Acknowledgments

This research was supported by National Science Foundation grant EAR-1427357. We are grateful to L. DeSmithers for the assistance in the field, to Orayëlle Chevrel, Elise Rumpf and Stephan Kolzenburg for constructive reviews and to Martha Savage for her editorial work.
Datasets are being prepared for publication in the USGS data repository (http://www.sciencebase.gov). In the meanwhile, it is available upon request. Any use of trade, firm, or product names is for descriptive purposes only and does not imply endorsement by the U.S. Government.

References

Anderson SW, McColley SM, Fink JH, Hudson RK (2005) The development of fluid

692 instabilities and preferred pathways in lava flow interiors: Insights from analog
693 experiments and fractal analysis. Geol Soc Am Spec Pap 396 2396:147–161. doi:
694 10.1130/0-8137-2396-5.147
695 Anderson SW, Smrekar SE, Stofan ER (2012) Tumulus development on lava flows: Insights
696 from observations of active tumuli and analysis of formation models. Bull Volcanol
697 74:931–946. doi: 10.1007/s00445-012-0576-2
698 Anderson SW, Stofan ER, Smrekar SE, et al (1999) Pulsed inflation of pahoehoe lava flows:
699 Implications for flood basalt emplacement. Earth Planet Sci Lett 168:7–18. doi:
700 10.1016/S0012-821X(99)00044-8
701 Behncke B, Fornaciai A, Neri M, et al (2016) Lidar surveys reveal eruptive volumes and rates
702 at Etna, 2007–2010. Geophys Res Lett 43:4270–4278. doi: 10.1002/2016GL068495
703 Calvari S, Pinkerton H (1999) Lava tube morphology on Etna and evidence for lava flow
704 emplacement mechanisms. J Volcanol Geotherm Res 90:263–280. doi: 10.1016/S0377-
705 0273(99)00024-4
706 Chevrel MO, Harris AJL, James MR, et al (2018) The viscosity of pāhoehoe lava: In situ syn-
707 eruptive measurements from Kilauea, Hawaii. Earth Planet Sci Lett 493:161–171. doi:
708 10.1016/j.epsl.2018.04.028
709 Davenport IJ, Holden N, Gurney RJ (2004) Characterizing errors in airborne laser altimetry
710 data to extract soil roughness. In: IEEE Transactions on Geoscience and Remote Sensing.
711 pp 2130–2141
712 de' Michieli Vitturi M, Tarquini S (2018) MrLavaLoba: A new probabilistic model for the
713 simulation of lava flows as a settling process. J Volcanol Geotherm Res 349:323–334. doi:
714 10.1016/j.jvolgeores.2017.11.016
715 Dietterich HR, Cashman K V (2014) Channel networks within lava flows: Formation,
716 evolution, and implications for flow behavior. J Geophys Res F Earth Surf 119:1704–
717 1724. doi: 10.1002/2014JF003103
718 Dietterich HR, Soule SA, Cashman K V, Mackey BH (2015) Lava Flows in 3D : Using
719 Airborne Lidar and Preeruptive Topography To Evaluate Lava Flow Surface Morphology
720 and Thickness in Hawai'i. Am Geophys Union Monogr 208:483–505. doi:
721 10.1002/9781118872079.ch22
722 Farquharson JI, James MR, Tuffen H (2015) Examining rhyolite lava flow dynamics through
723 photo-based 3D reconstructions of the 2011-2012 lava flowfield at Cordón-Caulle, Chile.
724 J Volcanol Geotherm Res 304:336–348. doi: 10.1016/j.jvolgeores.2015.09.004
725 Favalli M, Fornaciai A, Lormand C (2018) UAV-based remote sensing surveys of lava flow

726 fields : a case study from Etna ' s 1974 channel-fed lava flows. Bull Volcanol 80:1–18.
727 doi: 10.1007/s00445-018-1192-6
728 Favalli M, Fornaciai A, Mazzarini F, et al (2010) Evolution of an active lava flow field using a
729 multitemporal LIDAR acquisition. J Geophys Res Solid Earth 115:1–17. doi:
730 10.1029/2010JB007463
731 Fujita E, Hidaka M, Goto A, Umino S (2009) Simulations of measures to control lava flows.
732 Bull Volcanol 71:401–408. doi: 10.1007/s00445-008-0229-7
733 Glaze LS, Baloga SM, Fagents SA, Wright R (2014) The influence of slope breaks on lava flow
734 surface disruption. J Geophys Res Solid Earth 119:1837–1850. doi:
735 10.1002/2013JB010696
736 Gregg TKP (2017) Patterns and processes: Subaerial lava flow morphologies: A review. J
737 Volcanol Geotherm Res 342:3–12. doi: 10.1016/j.jvolgeores.2017.04.022
738 Gregg TKP, Fink JH (2000) A laboratory investigation into the effects of slope on lava flow
739 morphology. J Volcanol Geotherm Res 96:145–159. doi: 10.1016/S0377-0273(99)00148-
740 1
741 Gregg TKP, Keszthelyi LP (2004) The emplacement of pahoehoe toes: field observations and
742 comparison to laboratory simulations. Bull Volcanol 66:381–391. doi: 10.1007/s00445-
743 003-0319-5
744 Hamilton CW, Glaze LS, James MR, Baloga SM (2013) Topographic and stochastic influences
745 on pāhoehoe lava lobe emplacement. Bull Volcanol 75:1–16. doi: 10.1007/s00445-013-
746 0756-8
747 Harris AJ, Dehn J, James M, et al (2007) Pāhoehoe flow cooling, discharge, and coverage rates
748 from thermal image chronometry. Geophys Res Lett 34:1–6. doi: 10.1029/2007GL030791
749 Hoblitt RPR, Orr TTR, Heliker C, et al (2012) Inflation rates, rifts, and bands in a pāhoehoe
750 sheet flow. Geosphere 8:179–195. doi: 10.1130/GES00656.1
751 Hon K, Gansecki C, Kauahikaua J (2003) The transition from ʻaʻā to pāhoehoe crust on flows
752 emplaced during the Pu'u 'Ō'ō-Kūpaianaha eruption. USGS Prof Pap 1676 89–103. doi:
753 10.1016/0003-6870(73)90259-7
754 Hon K, Kauahikaua J, Delinger R, Mackay K (1994) Emplacement and inflation of pahoehoe
755 sheet flows: Observations and measurements of active lava flows on Kilauea Volcano,
756 Hawaii. Geol Soc Am Bull 106:351–370. doi: 10.1130/0016-
757 7606(1994)106<0351:EAIOPS>2.3.CO;2
758 James MR, Pinkerton H, Applegarth LJ (2009) Detecting the development of active lava flow
759 fields with a very-long-range terrestrial laser scanner and thermal imagery. Geophys Res

760 Lett 36:1–5. doi: 10.1029/2009GL040701
761 James MR, Pinkerton H, Ripepe M (2010) Imaging short period variations in lava flux. Bull
762 Volcanol 72:671–676. doi: 10.1007/s00445-010-0354-y
763 James MR, Pinkerton H, Robson S (2007) Image-based measurement of flux variation in distal
764 regions of active lava flows. Geochemistry, Geophys Geosystems 8:1–16. doi:
765 10.1029/2006GC001448
766 James MR, Robson S (2014) Sequential digital elevation models of active lava flows from
767 ground-based stereo time-lapse imagery. ISPRS J Photogramm Remote Sens 97:160–170.
768 doi: 10.1016/j.isprsjprs.2014.08.011
769 James MR, Robson S, Smith MW (2017) 3-D uncertainty-based topographic change detection
770 with structure-from-motion photogrammetry: precision maps for ground control and
771 directly georeferenced surveys. Earth Surf Process Landforms 42:1769–1788. doi:
772 10.1002/esp.4125
773 Katz MG, Cashman K V. (2003) Hawaiian lava flows in the third dimension: Identification and
774 interpretation of pahoehoe and ′a′a distribution in the KP-1 and SOH-4 cores.
775 Geochemistry, Geophys Geosystems 4:1–24. doi: 10.1029/2001GC000209
776 Kauahikaua J, Cashman K V., Mattox TN, et al (1998) Observations on basaltic lava streams
777 in tubes from Kilauea Volcano, island of Hawai'i. J Geophys Res Solid Earth 103:27303–
778 27323. doi: 10.1029/97JB03576
779 Kauahikaua J, Orr T, Patrick M, Trusdell F (2017) Steepest-Descent Lines for Kīlauea, Mauna
780 Loa, Hualālai, and Mauna Kea Volcanoes, Hawai'i. U.S. Geological Survey data release
781 Kolzenburg S, Favalli M, Fornaciai A, et al (2016) Rapid Updating and Improvement of
782 Airborne LIDAR DEMs Through Ground-Based SfM 3-D Modeling of Volcanic Features.
783 IEEE Trans Geosci Remote Sens 54:6687–6699. doi: 10.1109/TGRS.2016.2587798
784 Kolzenburg S, Giordano D, Thordarson T, et al (2017) The rheological evolution of the
785 2014/2015 eruption at Holuhraun, central Iceland. Bull Volcanol 79:. doi:
786 10.1007/s00445-017-1128-6
787 Kolzenburg S, Jaenicke J, Münzer U, Dingwell DB (2018) The effect of inflation on the
788 morphology-derived rheological parameters of lava flows and its implications for
789 interpreting remote sensing data - A case study on the 2014/2015 eruption at Holuhraun,
790 Iceland. J Volcanol Geotherm Res 357:200–212. doi: 10.1016/j.jvolgeores.2018.04.024
791 Macdonald GA (1953) Pahoehoe, aa, and block lava. Am. J. Sci. 251:169–191
792 Mattox TN, Heliker C, Kauahikaua J, Hon K (1993) Development of the 1990 Kalapana Flow
793 Field, Kilauea Volcano, Hawaii. Bull Volcanol 55:407–413. doi: 10.1007/BF00302000

Orr TR (2011) Lava tube shatter rings and their correlation with lava flux increases at Kīlauea Volcano, Hawai‘i. Bull Volcanol 73:335–346. doi: 10.1007/s00445-010-0414-3

Orr TR, Bleacher JE, Patrick MR, Wooten KM (2015) A sinuous tumulus over an active lava tube at Kīlauea Volcano: Evolution, analogs, and hazard forecasts. J Volcanol Geotherm Res 291:35–48. doi: 10.1016/j.jvolgeores.2014.12.002

Orr TR, Zoeller MH, Patrick MR, DeSmither LG (2017) GIS shapefiles for Kīlauea's episode 61g lava flow, Pu‘u ‘Ō‘ō eruption: May 2016 to May 2017. U.S. Geological Survey Data Release

Patrick M, Orr T, Anderson K, Swanson D (2019) Eruptions in sync: Improved constraints on Kīlauea Volcano's hydraulic connection. Earth Planet Sci Lett 507:50–61. doi: S0012821X18306897

Patrick M, Orr T, Fisher G, et al (2017) Thermal mapping of a pāhoehoe lava flow, Kīlauea Volcano. J Volcanol Geotherm Res 332:71–87. doi: 10.1016/j.jvolgeores.2016.12.007

Patrick MR, Kauahikaua J, Orr T, et al (2015) Operational thermal remote sensing and lava flow monitoring at the Hawaiian Volcano Observatory. In: Harris AJL, De Groeve T, Garel F, Carn SA (eds) Detecting, Modelling and Responding to Effusive Eruptions, Special Pu. Geological Society, London, p 15pp

Peterson DW, Swanson DA (1974) Observed formation of lava tubes. Stud Speleol 2:209–222

Peterson DW, Tilling RI (1980) Transition of basaltic lava from pahoehoe to aa, Kilauea Volcano, Hawaii: Field observations and key factors. J Volcanol Geotherm Res 7:271–293. doi: 10.1016/0377-0273(80)90033-5

Poland M, Orr TR, Kauahikaua JP, et al (2016) The 2014–2015 Pāhoa lava flow crisis at Kīlauea Volcano, Hawai ‘i: Disaster avoided and lessons learned. GSA Today 26:4–10

Poland MP (2014) Time-averaged discharge rate of subaerial lava at Kīlauea Volcano, Hawai'i, measured from TanDEM-X interferometry: Implications for magma supply and storage during 2011-2013. J Geophys Res Solid Earth. doi: 10.1002/2014JB011132

Rader E, Vanderkluysen L, Clarke A (2017) The role of unsteady effusion rates on inflation in long-lived lava flow fields. Earth Planet Sci Lett 477:73–83. doi: 10.1016/j.epsl.2017.08.016

Rumpf ME, Lev E, Wysocki R (2018) The influence of topographic roughness on lava flow emplacement. Bull Volcanol 80:63. doi: 10.1007/s00445-018-1238-9

Schaefer CJ, Kattenhorn SA (2004) Characterization and evolution of fractures in low-volume pahoehoe lava flows, eastern Snake River Plain, Idaho. Bull Geol Soc Am 116:322–336. doi: 10.1130/B25335.1

828 Scifoni S, Coltelli M, Marsella M, et al (2010) Mitigation of lava flow invasion hazard through
829 optimized barrier configuration aided by numerical simulation: The case of the 2001 Etna
830 eruption. J Volcanol Geotherm Res 192:16–26. doi: 10.1016/j.jvolgeores.2010.02.002
831 Self S, Keszthelyi L, Thordarson T (1998) The importance of Pahoehoe. Annu Rev Earth Planet
832 Sci 26:81–110. doi: 10.1146/annurev.earth.26.1.81
833 Sutton AJ, Elias T, Kauahikaua J (2003) Lava-effusion rates for the Pu'u'O'o–Kupaianaha
834 eruption derived from SO2 emissions and very low frequency (VLF) measurements. In:
835 Heliker CC, Swanson DA, Takahashi J (eds) The Pu'u 'O'o-Kupaianaha Eruption of
836 Kilauea Volcano, Hawai'i: The First 20 Years. U.S., U.S. Geolo. pp 137–148
837 Tarquini S, Coppola D (2018) Combined morphological and thermal analysis of lava flows: A
838 way to boost understanding of emplacement dynamics. Terra Nov 30:215–221. doi:
839 10.1111/ter.12328
840 Tarquini S, de' Michieli Vitturi M (2014) Influence of fluctuating supply on the emplacement
841 dynamics of channelized lava flows. Bull Volcanol 76:801. doi: 10.1007/s00445-014-
842 0801-2

843 Turner N, Houghton B, Taddeucci J, et al (2017a) Drone Peers into Open Volcanic Vents. Eos
844 98. doi: 10.1029/2017EO082751

845 Turner NR, Perroy RL, Hon K (2017b) Lava flow hazard prediction and monitoring with UAS:
846 a case study from the 2014–2015 Pāhoa lava flow crisis, Hawai'i. J Appl Volcanol 6:. doi:
847 10.1186/s13617-017-0068-3
848 Walker GPL (1973) Lengths of Lava Flows. Philos Trans R Soc A Math Phys Eng Sci 274:107–
849 118. doi: 10.1098/rsta.1948.0007
850 Walker GPL (1991) Structure, and origin by injection of lava under surface crust, of tumuli,
851 "lava rises", "lava-rise pits", and "lava-inflation clefts" in Hawaii. Bull Volcanol 53:546–
852 558. doi: 10.1007/BF00298155
853 Wentworth CK, Macdonald GA (1953) Structures and forms of basaltic rocks in Hawaii. US
854 Geol Surv Bull 994:98 pp. doi: 10.1101/lm.045484.117.25
855 Whelley PL, Garry WB, Hamilton CW, Bleacher JE (2017) LiDAR-derived surface roughness
856 signatures of basaltic lava types at the Muliwai a Pele Lava Channel, Mauna Ulu, Hawai'i.
857 Bull Volcanol 79:75. doi: 10.1007/s00445-017-1161-5
858 Whelley PL, Glaze LS, Calder ES, Harding DJ (2014) LiDAR-Derived Surface Roughness
859 Texture Mapping: Application to Mount St. Helens Pumice Plain Deposit Analysis. IEEE
860 Trans. Geosci. Remote Sens. 52:426–438
861